



HAL
open science

Black-Hole-to-Halo Mass Relation From UNIONS Weak Lensing

Qinxun Li, Martin Kilbinger, Wentao Luo, Kai Wang, Huiyuan Wang, Anna Wittje, Hendrik Hildebrandt, Ludovic van Waerbeke, Michael J Hudson, Samuel Farrens, et al.

► **To cite this version:**

Qinxun Li, Martin Kilbinger, Wentao Luo, Kai Wang, Huiyuan Wang, et al.. Black-Hole-to-Halo Mass Relation From UNIONS Weak Lensing. *Astrophys.J.Lett.*, 2024, 969 (2), pp.L25. 10.3847/2041-8213/ad58b0 . hal-04481443

HAL Id: hal-04481443

<https://hal.science/hal-04481443v1>

Submitted on 30 Nov 2024

HAL is a multi-disciplinary open access archive for the deposit and dissemination of scientific research documents, whether they are published or not. The documents may come from teaching and research institutions in France or abroad, or from public or private research centers.

L'archive ouverte pluridisciplinaire **HAL**, est destinée au dépôt et à la diffusion de documents scientifiques de niveau recherche, publiés ou non, émanant des établissements d'enseignement et de recherche français ou étrangers, des laboratoires publics ou privés.



Distributed under a Creative Commons Attribution 4.0 International License



Black Hole–Halo Mass Relation from UNIONS Weak Lensing

Qinxun Li^{1,2}, Martin Kilbinger³, Wentao Luo^{1,4}, Kai Wang⁵, Huiyuan Wang^{1,6}, Anna Wittje⁷, Hendrik Hildebrandt⁷, Ludovic Van Waerbeke⁸, Michael J. Hudson^{9,10,11}, Samuel Farrens³, Tobías I. Liaudat¹², Huiling Liu¹, Ziwen Zhang^{1,3}, Qingqing Wang¹, Elisa Russier^{3,13}, Axel Guinot¹⁴, Lucie Baumont³, Fabian Hervás Peters³, Thomas de Boer¹⁵, Jiaqi Wang¹⁶, Alan McConnachie¹⁷, Jean-Charles Cuillandre³, and Sébastien Fabbro¹⁷

¹ CAS Key Laboratory for Research in Galaxies and Cosmology, Department of Astronomy, University of Science and Technology of China, Hefei, Anhui 230026, People's Republic of China; qinxunli@ustc.edu

² Department of Physics and Astronomy, University of Utah, Salt Lake City, UT 84102, USA

³ Université Paris-Saclay, Université Paris Cité, CEA, CNRS, AIM, 91191, Gif-sur-Yvette, France; martin.kilbinger@cea.fr

⁴ Institute of Deep Space Sciences, Deep Space Exploration Laboratory, Hefei, 230026, People's Republic of China; wluo@ustc.edu.cn

⁵ The Kavli Institute for Astronomy and Astrophysics, Peking University, Beijing, People's Republic of China

⁶ School of Astronomy and Space Science, University of Science and Technology of China, Hefei 230026, People's Republic of China

⁷ Ruhr University Bochum, Faculty of Physics and Astronomy, Astronomical Institute (AIRUB), German Centre for Cosmological Lensing, 44780 Bochum, Germany

⁸ Department of Physics and Astronomy, University of British Columbia, Vancouver, BC V6T 1Z1, Canada

⁹ Department of Physics and Astronomy, University of Waterloo, Waterloo, ON N2L 3G1, Canada

¹⁰ Waterloo Centre for Astrophysics, University of Waterloo, Waterloo, ON N2L 3G1, Canada

¹¹ Perimeter Institute for Theoretical Physics, Waterloo, ON N2L 2Y5, Canada

¹² IRFU, CEA, Université Paris-Saclay, F-91191, Gif-sur-Yvette, France

¹³ Lawrence Berkeley National Laboratory, 1 Cyclotron Road, Berkeley, CA 94720, USA

¹⁴ Université Paris Cité, CNRS, Astroparticule et Cosmologie, F-75013 Paris, France

¹⁵ Institute for Astronomy, University of Hawaii, 2680 Woodlawn Drive, Honolulu, HI 96822, USA

¹⁶ Department of Astronomy, School of Physics and Astronomy, Shanghai Jiao Tong University, Shanghai 200240, People's Republic of China

¹⁷ NRC Herzberg Astronomy & Astrophysics, 5071 West Saanich Road, British Columbia, V9E2E7, Canada

Received 2024 February 16; revised 2024 June 7; accepted 2024 June 14; published 2024 July 2

Abstract

This Letter presents, for the first time, direct constraints on the black hole–halo mass relation using weak gravitational-lensing measurements. We construct type I and type II active galactic nucleus (AGN) samples from the Sloan Digital Sky Survey, with a mean redshift of 0.4 (0.1) for type I (type II) AGNs. This sample is cross correlated with weak-lensing shear from the Ultraviolet Near Infrared Optical Northern Survey. We compute the excess surface mass density of the halos associated with 36,181 AGNs from 94,308,561 lensed galaxies and fit the halo mass in bins of black hole mass. We find that more massive AGNs reside in more massive halos. The relation between halo mass and black hole mass is well described by a power law of slope 0.6 for both type I and type II samples, in agreement with models that link black hole growth to baryon feedback. We see no dependence on AGN type or redshift in the black hole–halo mass relation below a black hole mass of $10^{8.5} M_{\odot}$. Above that mass, we find more massive halos for the low- z type II sample compared to the high- z type I sample, but this difference may be interpreted as systematic error in the black hole mass measurements. Our results are consistent with previous measurements for non-AGN galaxies. At a fixed black hole mass, our weak-lensing halo masses are consistent with galaxy rotation curves but significantly lower than galaxy-clustering measurements. Finally, our results are broadly consistent with state-of-the-art hydrodynamical cosmological simulations, providing a new constraint for black hole masses in simulations.

Unified Astronomy Thesaurus concepts: Galaxy dark matter halos (1880); Gravitational lensing (670); Active galactic nuclei (16); Supermassive black holes (1663); Galaxies (573)

1. Introduction

Supermassive black holes (SMBHs), with typical masses of 10^6 – $10^{10} M_{\odot}$, are among the most mysterious objects in the Universe. It is widely accepted that most galaxies have an SMBH in their center (Kormendy & Richstone 1995). Though the formation and evolution of SMBHs remain unclear, there is already a large amount of evidence indicating a coevolution between SMBHs and their host galaxies (see, for a review, Kormendy & Ho 2013). In addition, galaxy properties are expected and have been shown to be closely related to their host dark-matter halos as this is where they form and evolve (e.g., Wechsler & Tinker 2018). These observational results

suggest that a close connection between halos, galaxies, and SMBHs needs to be established to understand the coevolution of these different classes of objects (H. Zhang et al. 2023, 2024). The gravitational potential of a halo determines the accretion of baryons and star formation of galaxies onto the halo. Several mechanisms in galaxies, such as bar instabilities, conduct cold gas into galaxy centers, feeding the accretion of SMBHs. The energetic feedback of the accretion can push baryons outside the galaxy or even the halo, which will suppress the SMBH growth and star formation. Such complex interplay among halos, galaxies, and SMBHs plays a crucial role in galaxy formation and evolution and is still under exploration.

The first step toward understanding the connection between halos, galaxies, and SMBHs is to build statistical relationships between these three types of objects based on observational data. Much effort has been devoted to this aspect in previous decades. The pioneering work was initiated by Dressler &

Richstone (1988), who noted a positive correlation between the black hole mass and the spheroid luminosity. Subsequent studies with more extensive data sets found a tight correlation between black hole mass M_* and various galaxy properties, such as bulge mass and stellar velocity dispersion, across several orders of magnitude (Magorrian et al. 1998; Ferrarese & Merritt 2000; Gebhardt et al. 2000; Kormendy & Ho 2013; Saglia et al. 2016). There are also many studies on the galaxy–halo scaling relations, with the stellar mass–halo mass relation (see Yang et al. 2008) as a representative example.

The relation between SMBHs and their host halos has yet to be extensively studied. Ferrarese (2002) used the maximum rotational velocity of late-type galaxies, v_c , as a tracer of the halo mass and the central velocity dispersion, σ_* , of their bulges as a tracer of the black hole mass. This led to the first measurement of the M_* – M_h relation. This relation for galaxies was further confirmed in larger samples (Baes et al. 2003; Pizzella et al. 2005; Volonteri et al. 2011) with a similar method, which used σ_* and v_c as tracers of black hole and halo mass. Sabra et al. (2015), Davis et al. (2019), and Marasco et al. (2021) used direct dynamical black hole mass instead of σ_* and found a correlation between SMBH mass and dynamical halo mass. These works based on dynamics are limited to small galaxy samples and rely on strong assumptions about the kinematic state of the gas and the density profile of the dark-matter halo. There is also evidence for the opposite idea that the SMBH mass does not correlate with halo mass, as seen in bulgeless galaxies (Kormendy & Bender 2011).

Unlike quiescent SMBHs in normal galaxies, active galactic nuclei (AGNs) are SMBHs that are actively accreting matter. The trigger, growth, and feedback of AGNs are critical issues in the halo–galaxy–SMBH connection. For the M_* – M_h relation in AGN samples, the halo mass in different bins of M_* is typically inferred from the spatial two-point correlation function of AGNs together with empirical models such as halo occupation distribution (HOD) and abundance matching (e.g., Krumpel et al. 2015, 2023; Powell et al. 2018, 2022; Shankar et al. 2020). Using gas dynamics, the M_* – M_h relation has been measured from $z = 0$ to $z = 6$ using reverberation mapping and virial black hole masses (Shimasaku & Izumi 2019; Robinson et al. 2021). More massive AGNs were more likely found in more massive halos. However, the methods used to estimate the halo mass in the works listed above are indirect and strongly model dependent.

Gravitational lensing, an effect directly related to the density field, has been emerging as the most direct and clean method to measure halo mass (Mandelbaum et al. 2006; Luo et al. 2018). For galaxies, Bandara et al. (2009) and Z. Zhang et al. (2024) inferred black hole masses from the M_* – σ_* relation, and measured halo masses with strong lensing and weak lensing, respectively. Their results significantly differ from the M_* – M_h relation from AGN clustering. Previous weak-lensing studies on AGNs focused on the M_* – M_h relation, using samples with limited size (Leauthaud et al. 1874; Mandelbaum et al. 2009; Luo et al. 2022). In this work, we use, for the first time, weak lensing to constrain the AGN M_* – M_h relation. We utilize the Sloan Digital Sky Survey (SDSS) AGN sample together with the galaxy shape catalog derived from the Ultraviolet Near Infrared Optical Northern Survey (UNIONS) imaging data, achieving a high signal-to-noise ratio measurement of the M_* – M_h relation.

This Letter is organized as follows: Section 2 introduces the AGN lens samples and weak-lensing galaxy shape catalogs,

and Section 3 presents our methodology before we show and discuss our results in Section 4.

Throughout this work, we assume a Planck18 cosmology (Planck Collaboration et al. 2020), with $H_0 = 67.7 \text{ km s}^{-1} \text{ Mpc}^{-1}$, $\Omega_m = 0.31$, $\Omega_\Lambda = 0.69$, and $\sigma_8 = 0.81$.

2. Data

2.1. Lens Sample

In this work, we construct type I and type II AGN/quasar samples as our lens samples based on three SDSS spectroscopic catalogs, described in the following sections.

2.1.1. SDSS Type I AGNs

Based on the SDSS Data Release 16 quasar catalog (Lyke et al. 2020), Wu & Shen (2022) fitted the spectrum of 750,414 quasars in the redshift range $0.1 < z < 6$ and measured virial black hole masses. As an update to Shen et al. (2011), they used the FWHM of $H\beta$, Mg II, and C IV broad emission lines (combined with the broad-line-region radius inferred from continuum luminosity) for their estimates. Here, we adopt their black hole masses based on $H\beta$. The mean statistical error in $\log M_*$ is much smaller than the systematic error of the virial black hole mass (~ 0.4 dex; see Shen 2013).

As a complement to Wu & Shen (2022) at low black hole masses, we use the AGN catalog from Liu et al. (2019), a complete AGN sample including both quasars and Seyfert galaxies from SDSS Data Release 7. Black hole masses are measured with $H\alpha$ and $H\beta$, and we adopt the $H\beta$ mass. This catalog contains 14,584 AGNs at $z < 0.35$.

We merge the two catalogs and remove duplicate objects. We perform several consistency tests of the black hole masses from two different catalogs, which are described in Appendix B in detail. In this work, we use AGNs with redshifts $0.05 < z < 0.6$ in the overlapping sky region between SDSS and UNIONS, resulting in 14,649 lenses, 3 times larger than the sample size of previous type I AGN weak-lensing studies (Luo et al. 2022). We divide the sample into low ($\log M_*/M_\odot < 7.9$), medium ($7.9 < \log M_*/M_\odot < 8.5$), and high ($\log M_*/M_\odot > 8.5$) black hole mass bins. We introduce a weight $w_{1,\text{nofz}}$ such that the weighted redshift distributions of the low- and medium-mass bins equal the high-mass bin. This allows for a fair comparison between the mass bins free of redshift evolution or selection biases. The weighted average redshift of each bin is 0.4, and the weighted distributions of the three bins are shown in Figure 1.

2.1.2. SDSS Type II AGNs

In addition to the type I catalog, we construct a type II AGN sample from the SDSS Data Release 8 Max-Planck Institute für Astrophysik–Johns Hopkins University (MPA–JHU) catalog (Kauffmann et al. 2003; Brinchmann et al. 2004). We identify galaxies classified as AGNs using the Baldwin–Phillips–Terlevich diagram (Baldwin et al. 1981) within the catalog. We estimate black hole masses from the velocity dispersion using the M_* – σ_* relation proposed by Saglia et al. (2016). To correct for the aperture effect of velocity dispersion, we adopt the method outlined by Cappellari et al. (2006): First, we cross-match the sample with the New York University Value-Added Galaxy Catalog (NYU-VAGC; Blanton et al. 2005) to obtain the r -band effective radius R_e . Subsequently, we

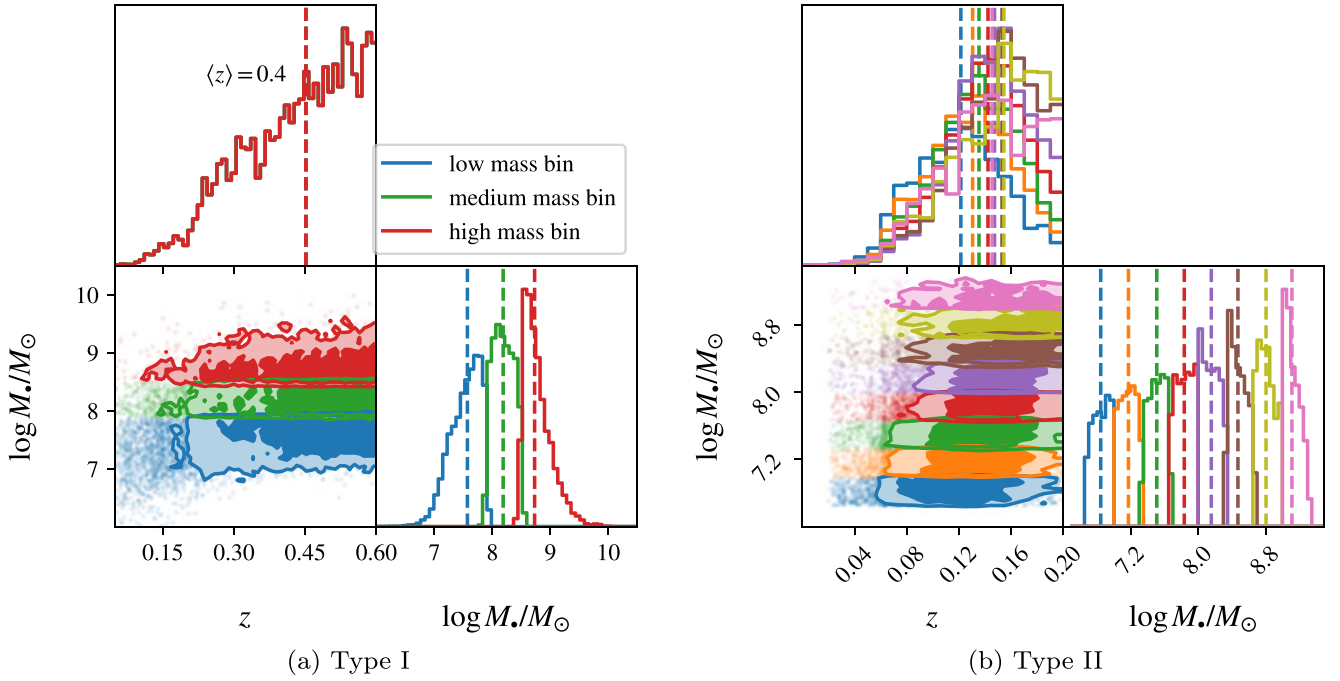


Figure 1. Panel (a): the weighted joint and marginalized redshift and black hole mass distribution of the type I samples. Low, medium, and high black hole mass bins are shown in blue, green, and red, respectively. We use the redshift-distribution weights $w_{1,\text{no}fz}$ and the lensing efficiency weights $(\Sigma_{\text{cr}}^{-1})^2$ for the 1D and 2D distributions. For comparison, the points show the 2D distribution before weighting. The three weighted 1D redshift histograms overlap. Panel (b): as panel (a) but for the type II samples and without redshift-distribution weighting.

compute the aperture-corrected velocity dispersion, σ_* , using the formula $\sigma_* = \sigma_{\text{ap}}(R_e/R_{\text{ap}}/8)^{-0.066}$, where σ_{ap} is the fiber velocity dispersion and $R_{\text{ap}} = 3''$ is the fiber aperture for SDSS spectra. We perform tests to estimate the systematic error from the aperture correction, which is detailed in Appendix B.2. Finally, we restrict the sample to 21,532 AGNs within the redshift range $z \in [0.02, 0.2]$, black hole mass range $\log M./M_\odot \in [6.67, 9.33]$, and within the UNIONS footprint. The type II sample exhibits lower redshifts ($\langle z \rangle \simeq 0.13$) than the type I sample. Because of that, the number of lensed background galaxies is higher with less dilution by foreground galaxies, resulting in a higher average lensing efficiency. We separate the type II sample into eight mass bins. We do not perform weighting to the type II sample because the redshift range of the type II sample is narrow and the difference in average redshift among black hole mass bins is small.

2.2. Source Sample

The shape catalogs serving as the background source sample in this work are the v1.3 ShapePipe and v1.0 *lensfit* catalogs of UNIONS.¹⁸ UNIONS is an ongoing multiband wide-field imaging survey conducted with three telescopes (Canada–France–Hawai‘i Telescope for u and r bands, Subaru telescope for g and z bands, and Pan-STARRS for the i band) in Hawai‘i. UNIONS will cover 4800 deg² of the northern sky with deep exposures and high-quality images. The depth (limiting magnitude with point source 5σ in a $2''$ diameter aperture) reaches 24.3, 25.2, 24.9, 24.3, and 24.1 in u , r , g , i , and z , respectively.

At the time when the shear catalogs were produced (beginning of 2022), the survey covered an area of around 3500 deg² in the r band (the galaxy shapes were measured in this band). The overlapping region between UNIONS and

SDSS is about 2000 deg². We do not have photometric redshifts for each source galaxy in the catalog at this stage of the UNIONS processing since the observations and calibration of the multiband photometry are still ongoing. Instead, we estimated the overall redshift distribution by a method based on self-organizing maps (SOMs). See Appendix A for more details about photometric redshifts.

The ShapePipe catalog was processed with the SHAPEPIPE software package (Farrens et al. 2022). It contains 98 million galaxies over an effective area of 3200 deg². An earlier version of the ShapePipe catalog was published in Guinot et al. (2022). Some updates in processing were implemented for the v1.3 shear catalog used here as follows. First, to model the point-spread function (PSF), instead of PSFEX (Bertin 2011) we used an MCCD (Liaudat et al. 2021) that performs a nonparametric multi-CCD fit of the PSF over the entire focal plane. Liaudat et al. (2021) showed that MCCD provides a less noisy PSF model with smaller ellipticity residuals compared to PSFEX. Second, we reduced the minimum area to detect an object from 10 to 3 pixels via the SExtractor configuration keyword DETECT_MINAREA = 3. This leads to a smaller galaxy selection bias on the ensemble shear estimates. Third, we added the section on the relative size between galaxies, T_{gal} , and the PSF, T_{PSF} , as $T_{\text{gal}}/T_{\text{PSF}} < 3$ to avoid contamination by very diffuse, mostly low signal-to-noise objects, which tend to be artifacts.

The *lensfit* shape catalog was created with the THELI processing and *lensfit* software (Miller et al. 2007). It contains 109 million galaxies in a 2100 deg² sky area. The effective area and number density of the ShapePipe and *lensfit* catalogs are different due to masking and processing choices. In the following, we use the more conservative *lensfit* mask for both shape catalogs, defining the common UNIONS footprint in which SDSS AGNs are selected. Both *lensfit* and ShapePipe catalogs are based on the same image data.

¹⁸ <https://www.skysurvey.cc/>

3. Methods

3.1. Galaxy–Galaxy Lensing Technique

Galaxy–galaxy lensing denotes the shape distortions of background source galaxies due to the gravitational field of matter associated with foreground lens galaxies (see, for a review, Kilbinger 2015). The main *physical* quantity related to galaxy–galaxy lensing is the excess surface density (ESD) $\Delta\Sigma$, at a projected distance R , defined as the mean surface density within a disk of radius R minus a boundary term, which is the mean surface mass at radius R ,

$$\Delta\Sigma(R) = \bar{\Sigma}(<R) - \Sigma(R). \quad (1)$$

The main *observable* for galaxy–galaxy lensing is the tangential shear, γ_t , of a source sample induced by a lens at projected distance R . This observable is related to the ESD via

$$\Delta\Sigma(R) = \Sigma_{\text{cr}} \gamma_t(R), \quad (2)$$

where the critical surface mass density Σ_{cr} is defined for a single lens–source pair as

$$\Sigma_{\text{cr}}(z_l, z_s) = \frac{c^2}{4\pi G} \frac{d(z_s)}{d(z_l) d(z_l, z_s)} \frac{1}{(1 + z_l)^2}. \quad (3)$$

Here, z_s (z_l) is the source (lens) redshift, and $d(z_s)$, $d(z_l)$, and $d(z_l, z_s)$ are the angular diameter distance from the observer to the source, to the lens, and the lens–source distance, respectively. The constants are the speed of light c and the Newtonian gravitational constant G .

3.2. Estimators

An estimator for the tangential shear of a background source sample around a lens galaxy population is

$$\langle \gamma_t(R) \rangle = \frac{\sum_{\text{ls}} w_l w_s \epsilon_{t,s} 1_{b(R)}(|\mathbf{r}_l - \mathbf{r}_s|)}{\sum_{\text{ls}} w_l w_s}. \quad (4)$$

This estimator is a weighted sum over the observed tangential ellipticities, $\epsilon_{t,s}$, of source galaxies around lens galaxies. Source galaxies have a weight, w_s , stemming from the galaxy shape estimation that indicates measurement uncertainties. Lens weights, $w_l \equiv w_{l,\text{nofz}}$, are introduced to homogenize the redshift distribution across lens samples as discussed in Section 2.2. The indicator function $1_S(x)$ of the set S is unity if $x \in S$ and zero otherwise. In Equation (4), this function selects galaxy pairs in a bin $b(R)$ around the projected separation R of the pair, and thus the sum is carried out over all lens–source pairs in the given annular bin. The binning scheme encoded in $b(R)$ defines 15 logarithmic bins between $0.02 \text{ Mpc } h^{-1}$ and $20 \text{ Mpc } h^{-1}$.

Since we do not have photometric redshifts of individual background galaxies in the shape catalog, we compute an effective surface mass density by averaging Equation (3) over the source redshift distribution. Inserting this effective value into Equation (2) results in an average excess surface mass density. Since we cannot select sources to be strictly behind the lens sample, this leads to a divergence of Σ_{cr} when $z_s \rightarrow z_l$. A practical solution is to compute the inverse effective critical surface mass density,

$$\overline{\Sigma_{\text{cr}}^{-1}}(z_l) = \frac{4\pi G}{c^2} d(z_l) (1 + z_l)^2 \int_{z_l}^{z_{\text{lim}}} dz_s n(z_s) \frac{d(z_l, z_s)}{d(z_s)}, \quad (5)$$

where $z_{\text{lim}} = 5$ is the upper limit of the redshift distribution. This quantity is the inverse of the critical surface mass density Σ_{cr} , as defined in Equation (3), weighted by the source redshift distribution (see Section 2). The effective excess surface mass density is then

$$\overline{\Delta\Sigma}(R) = \gamma_t [\overline{\Sigma_{\text{cr}}^{-1}}(z_l)]^{-1}. \quad (6)$$

Using Equation (5), a first estimator for the excess surface mass density is readily derived as

$$\langle \overline{\Delta\Sigma}(R) \rangle = \frac{\sum_{\text{ls}} w_l w_s \epsilon_{t,s} [\overline{\Sigma_{\text{cr}}^{-1}}(z_l)]^{-1} 1_{b(R)}(|\mathbf{r}_l - \mathbf{r}_s|)}{\sum_{\text{ls}} w_l w_s}. \quad (7)$$

When using the effective surface mass density, the weights for a given lens can be updated by multiplication with the square of the inverse effective critical surface mass density Equation (3) to downweigh lenses with a low lensing efficiency, $w_l \rightarrow w_l (\overline{\Sigma_{\text{cr}}^{-1}}(z_l))^2$. With this, we write our final estimator of the excess surface mass density as

$$\langle \overline{\Delta\Sigma}(R) \rangle = \frac{\sum_{\text{ls}} w_l \overline{\Sigma_{\text{cr}}^{-1}}(z_l) w_s \epsilon_{t,s} 1_{b(R)}(|\mathbf{r}_l - \mathbf{r}_s|)}{\sum_{\text{ls}} w_l w_s (\overline{\Sigma_{\text{cr}}^{-1}}(z_l))^2}. \quad (8)$$

The covariance matrix is estimated using the bootstrap method, for which we perform resampling 5000 times for each measurement. We also conduct a series of systematic tests and apply the boost factor correction $\langle \overline{\Delta\Sigma}(R)^c \rangle = B(R) \langle \overline{\Delta\Sigma}(R) \rangle$. We refer to Appendix C for details.

3.3. AGN Lens Model

Our lens sample contains both central and satellite AGN host galaxies, and we need to consider contributions to the ESD from both. We adopt an HOD model from Guzik & Seljak (2002) to describe the average ESD around the AGN sample,

$$\Delta\Sigma = \Delta\Sigma_b + (1 - f_{\text{sat}}) \Delta\Sigma_{\text{h, cen}} + f_{\text{sat}} \Delta\Sigma_{\text{h, sat}} + \Delta\Sigma_{2\text{h}}, \quad (9)$$

where f_{sat} is the satellite galaxy fraction of the sample, left as a free parameter. $\Delta\Sigma_b$ is the contribution from baryons in the host galaxy, containing the stellar mass M_* . $\Delta\Sigma_{\text{h, cen}}$ and $\Delta\Sigma_{\text{h, sat}}$ are the one-halo terms of the central and satellite galaxy, respectively. $\Delta\Sigma_{2\text{h}}$ is the two-halo term. The terms are described in Appendix D in detail.

To fit the ESDs with the lens model, we use the EMCEE package (Foreman-Mackey et al. 2013) to perform Markov Chain Monte Carlo inference. We adopt a Gaussian likelihood function and flat priors. We run 2000 steps with 20 walkers and use the 16th–84th percentiles of the posterior distribution to estimate the parameter errors.

4. Results and Discussion

4.1. AGN Black Hole–Halo Mass Relation

The measured galaxy–galaxy lensing ESD profiles for the type I sample are shown in Figure 2. We measure the ESD with a high significance. The signal-to-noise ratio, taken as $\sum_i \Delta\Sigma_i^2 \sigma_i^{-2}$, where σ_i^2 is the variance of the i th radial bin (we check the covariance matrices and find them very diagonal), from ShapePipe (*lensfit*) is 52 (80), 59 (70), and 68 (78) in the three bins, respectively. Our measurements are well reproduced by the HOD models with three free

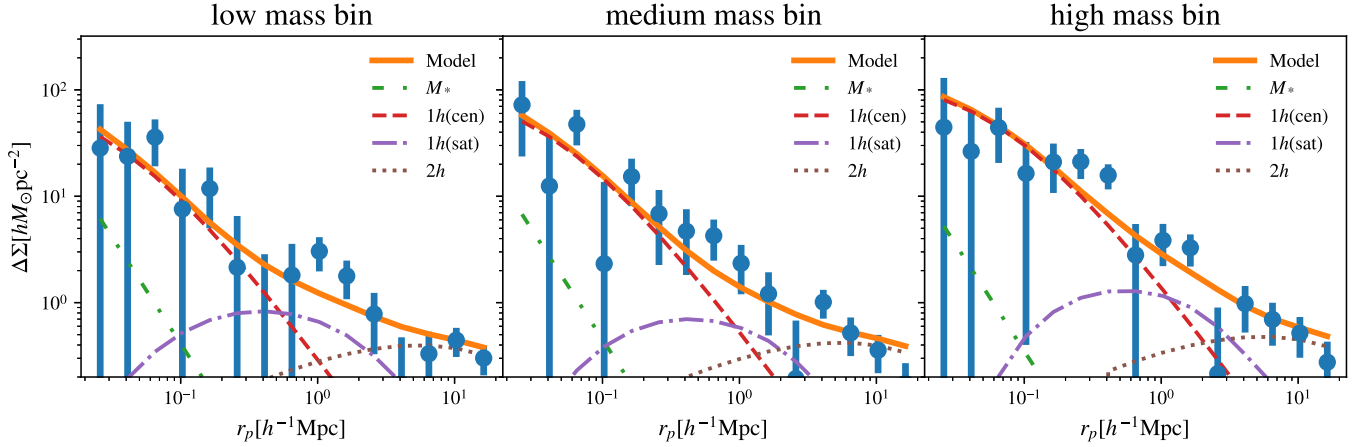


Figure 2. Galaxy–galaxy lensing excess surface mass density of three black hole mass bins from ShapePipe. The best-fit HOD models are presented in orange lines. The baryon contribution, one-halo term of centrals, one-halo term of satellites, and two-halo term are plotted in green, red dashed, purple dashed–dotted, and brown dotted lines, respectively. The measurements from the *lensfit* catalog are similar.

parameters. The amplitude of the ESD increases with M_* , indicating that more massive SMBHs are situated in more massive halos. A similar trend is observed in the type II sample.

The top left panel of Figure 3 shows our M_* – M_h relation from the ShapePipe catalog. Systematic errors in the shape measurements contribute to the total error budget at a comparable level to statistical errors, as indicated by the disparity between the type I ShapePipe and *lensfit* results in the top right panel. This underscores the robustness of our analysis across different shape catalogs.

We observe that more massive AGNs inhabit larger dark-matter halos (the *lensfit* results are flatter than ShapePipe, but they are consistent). We fit the type I and type II results with a power-law model:

$$\log M_h = a \log M_* + b \quad (10)$$

and get $a = 0.60 \pm 0.24$, $b = 7.37 \pm 1.96$ for type I and $a = 0.58 \pm 0.06$, $b = 7.80 \pm 0.47$ for type II, respectively. Their slopes are consistent. The slope $a \sim 0.6$ is consistent with the argument of the theoretical models with an assumption that the growth of black holes are limited by AGN feedback (Mo et al. 2023; Voit et al. 2024):

$$M_* \propto E_B \propto M_{\text{bulge}} \sigma_*^2 \propto \sigma_*^5 \propto M_h^{5/3}, \quad (11)$$

where E_B and M_{bulge} are the binding energy and mass of the bulge, respectively.

In our results, both type I and type II samples exhibit similar M_* – M_h relations despite their distinct classifications and redshift ranges. Although they have different normalization in a power-law fit, the type I bins are consistent with type II below a black hole mass of $10^{8.5} M_\odot$. At higher black hole masses, type I AGNs have a lower halo mass compared to type II. This difference may be interpreted as the systematic error in either the type I or type II black hole mass estimation. For type II, the aperture correction of the velocity dispersion contributes to the systematics (Zhu et al. 2023). For type I, the slope of the size–luminosity relation is not very well determined (Du & Wang 2019). As an example, recent spectroscopic interferometer measurements (GRAVITY Collaboration et al. 2024) of the AGN size–luminosity relation, upon which the virial mass measurement of type I AGNs relies, exhibit a shallower slope than the one proposed by Bentz et al. (2006) from reverberation

mapping if the difference in broad-line region size between $H\beta$ and $\text{Pa}\alpha$ is taken into account with the prescriptions from photoionization models. Our type I black hole masses are calculated by Wu & Shen (2022) using the $H\beta$ prescription from Vestergaard & Peterson (2006), which is based on Bentz et al. (2006). To account for the new measurements of GRAVITY Collaboration et al. (2024), we use their size–luminosity slope (adjusted for $H\beta$) $\alpha = 0.30 \pm 0.19$ to derive a black hole mass prescription with the same sample and the same method as Vestergaard & Peterson (2006) and get the updated relation

$$\log \left(\frac{M_*}{M_\odot} \right) = 6.88 + 2 \log \left(\frac{\text{FWHM}_{H\beta}}{1000 \text{ km s}^{-1}} \right) + 0.30 \log \left(\frac{\lambda L_{5100}}{10^{44} \text{ erg s}^{-1}} \right), \quad (12)$$

where $\log \lambda L_{5100}$ is the luminosity of the continuum at 5100 \AA . We then adjust the average black hole mass of the type I sample, as shown in Figure 3. The black hole mass of the high-mass bin changes the most and moves the black hole–halo mass relation closer to the type II line. We caution that this shallower slope depends on the photoionization correction, which is only applied to some of the AGNs in the GRAVITY sample. In conclusion, we do not find evidence of type- or redshift-dependence in the M_* – M_h relationship, considering the systematic uncertainty of black hole mass measurement.

It is worth mentioning that a dip emerges at $\log M_*/M_\odot \simeq 8.1$ in the M_* – M_h relation for the type II sample. The dip is robust against several tests such as using the *lensfit* shape catalog and restricting the type II lens sample to central galaxies or early-type galaxies. We will further explore the dip in future work.

4.2. Comparison with Other Observations

The positive slope of our black hole–halo mass relation is consistent with previous findings from dynamical (Robinson et al. 2021) and clustering analyses (Krumpe et al. 2015; Shankar et al. 2020). Robinson et al. (2021) employed reverberation mapping to determine black hole masses and utilized H I FWHM to estimate halo masses for 24 local AGNs. Our results are consistent with Robinson et al. (2021) at low masses but at $\log M_*/M_\odot \simeq 8$, we find a lower halo mass. Our measured halo masses in the high-mass regime for both type I

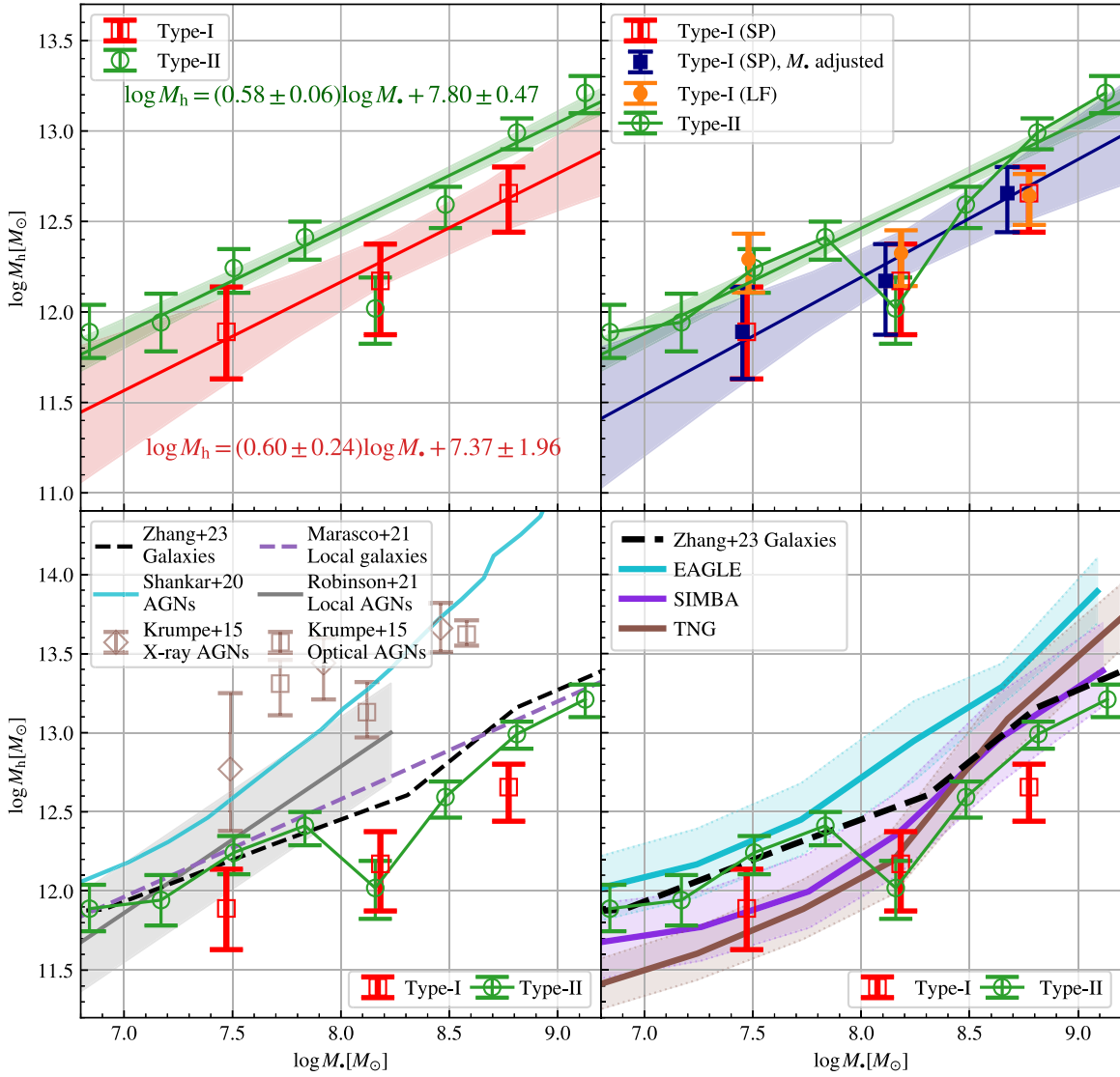


Figure 3. Black hole–halo mass relation. In all panels, the red squares and green circles are our type I and type II results from ShapePipe, respectively. Top left panel: the red and green shades are 1σ confidence intervals of the power-law fits. Top right: the filled navy squares are type I ShapePipe results with an adjustment on black hole mass. The filled orange circles correspond to the type I results with *lensfit*. Bottom left panel: comparison with observational results from the literature. Brown squares and rhombuses are AGN clustering results for optically selected and X-ray selected samples from Krump et al. (2015), respectively. Cyan and gray lines show AGN clustering and dynamics results from Shankar et al. (2020) and Robinson et al. (2021), respectively. Results for normal galaxies are shown as dashed lines (purple line from Marasco et al. 2021 and black line from Z. Zhang et al. 2024). Bottom right panel: results from EAGLE, TNG, and SIMBA hydrosimulations are shown in cyan, brown, and purple lines with 16th–84th percentiles displayed as shaded areas.

and type II samples are also systematically lower than the clustering results reported in Krump et al. (2015) and Shankar et al. (2020). The discrepancy between clustering and lensing halo masses was noticed in previous works (Mandelbaum et al. 2009). The clustering method leverages the monotonic relation between halo mass and halo bias, while weak lensing directly probes the matter overdensity around the tracers. It has long been known that the clustering strength of halos also depends on their secondary properties, such as the halo structure and the halo assembly history, which is called the halo assembly bias or the secondary halo bias (Gao & White 2007; Wang et al. 2024). Therefore, if the host galaxies of AGNs prefer to live in dark-matter halos with biased secondary properties, it will alter the clustering strength without changing the host halo mass, while lensing is free of this effect.

Furthermore, we compare our results to those of normal (non-AGN) galaxies. Marasco et al. (2021) measured halo

masses through globular cluster dynamics and galaxy rotation curves in 55 nearby galaxies with directly measured black hole masses. Z. Zhang et al. (2024) used the Dark Energy Camera Legacy Survey (Dey et al. 2019) and DECaLS shape catalog (Zhang et al. 2022) to measure galaxy–galaxy lensing of quiescent galaxies for $z < 0.2$ for different σ_* bins. We plot their result with black hole masses inferred from the M_* – σ_* relation of Saglia et al. (2016). Compared to these results, we find that both type I and type II are broadly consistent with normal galaxies, suggesting no intrinsic difference in the M_* – M_h relation between non-AGN galaxies and AGNs.

4.3. Constraint on Black Hole Mass in Simulations

In state-of-the-art cosmological hydrodynamical simulations, black hole growth fed by gas accretion is a crucial factor in driving AGN feedback, which, in turn, is a major mechanism to suppress star formation activities in massive galaxies (Davé et al. 2019).

However, these simulations cannot resolve the detailed accretion process. Instead, empirical subgrid recipes are employed to model this process, and the free parameters in these recipes need to be calibrated using observational scaling relations, such as the M_*-M_{h} relation (Habouzit et al. 2021).

However, we note that stellar mass itself is subject to several subgrid processes, including the stellar feedback and the AGN feedback, which makes the calibration process quite complicated. In contrast, halo masses are relatively robust and less sensitive to baryonic processes. Therefore, the black hole–halo mass relation is a better scaling relation for calibration of subgrid parameters in these simulations, and our work takes the first step to establish this relation in observation.

To compare our measurements with simulations, we used the RefL0100N1054 run for EAGLE (Schaye et al. 2015), the TNG100 run of The Next Generation Illustris simulations (IllustrisTNG; Springel et al. 2017), and the m100n1024 run for SIMBA (Davé et al. 2019). We calculated AGN luminosity from Equation (1) in Habouzit et al. (2021) and selected central subhalos with $L_{\text{BH}}/L_{\text{Edd}} > 0.001$ as the “AGN” sample in the simulation. We used the snapshot with $z \sim 0.4$, which is the average redshift of our type I AGN sample. We find no significant evolution between $z = 0.4$ and $z = 0.1$ in the three simulations, which is consistent with our observation. We also compared the “AGN” sample and central-galaxy sample in the simulation and found no statistically significant difference between their M_*-M_{h} relations. The AGN M_*-M_{h} relations from the three simulations are plotted in the lower right panel of Figure 3.

Although the three simulations calibrate their models to be in good agreement with observed relations (Kormendy & Ho 2013; McConnell & Ma 2013) between M_* and stellar mass of the galaxy, M_* , or of the bulge, M_{bulge} , their M_*-M_{h} relations do not perfectly match our measurements. The difference among the simulations under similar calibration clearly reflects how different black hole accretion and AGN feedback mechanisms shape the black hole masses in simulations. The predicted halo mass from EAGLE is consistent with ours at low masses but is significantly higher than ours at $\log M_*/M_{\odot} > 8$. However, TNG and SIMBA predict lower halo masses at fixed black hole masses compared to EAGLE, which are more consistent with our observations (both type I and type II). Among the three simulations, SIMBA has the M_*-M_{h} relation that is the closest to ours, with all differences within 1σ .

4.4. Future Prospects

Current data suffer from a small AGN sample size and limited accuracy of black hole mass estimation. Large spectroscopic surveys such as DESI (Levi et al. 2013) and PFS¹⁹ will provide larger quasar samples with reliable virial black hole mass measurements. Already now integral field spectroscopy and reverberation mapping observations are improving the virial black hole mass measurement accuracy. From the perspective of weak-lensing data, we will soon get the 4800 deg² shape catalog with photo- z from the completed UNIONS survey.

Future weak-lensing surveys such as Euclid (Euclid Collaboration et al. 2020), Rubin-LSST (Ivezić et al. 2019), Roman (Spergel et al. 2015), CSST (Gong et al. 2019), and WFST (WFST Collaboration et al. 2023), will provide galaxy samples with accurate shape measurements to higher redshifts,

covering larger sky areas. This will enable us to measure the M_*-M_{h} relation with higher accuracy, as well as its dependency on the host-galaxy properties.

Acknowledgments

We thank Eric Jullo, Shiming Gu, Zheng Zheng, and Chris Miller for their helpful discussion.

The authors thank the support from the National Natural Science Foundation of China (No. 12192224, 11833005, 11890693), the National Key R&D Program of China (2021YFC2203100), the 111 project for “Observational and Theoretical Research on Dark Matter and Dark Energy” (B23042), CAS Project for Young Scientists in Basic Research, grant No. YSBR-062. H.H. is supported by a DFG Heisenberg grant (Hi 1495/5-1), the DFG Collaborative Research Center SFB1491, as well as an ERC Consolidator Grant (No. 770935). A.W. is also supported by SFB1491.

We are honored and grateful for the opportunity of observing the Universe from Maunakea and Haleakala, which both have cultural, historical and natural significance in Hawai’i. This work is based on data obtained as part of the Canada–France Imaging Survey, a CFHT large program of the National Research Council of Canada and the French Centre National de la Recherche Scientifique. Based on observations obtained with MegaPrime/MegaCam, a joint project of CFHT and CEA Saclay, at the Canada–France–Hawaii Telescope (CFHT) which is operated by the National Research Council (NRC) of Canada, the Institut National des Science de l’Univers (INSU) of the Centre National de la Recherche Scientifique (CNRS) of France, and the University of Hawaii. This research used the facilities of the Canadian Astronomy Data Centre operated by the National Research Council of Canada with the support of the Canadian Space Agency. This research is based in part on data collected at Subaru Telescope, which is operated by the National Astronomical Observatory of Japan. Pan-STARRS is a project of the Institute for Astronomy of the University of Hawai’i, and is supported by the NASA SSO Near Earth Observation Program under grants 80NSSC18K0971, NNX14AM74G, NNX12AR65G, NNX13AQ47G, NNX08AR22G, 80NSSC21K1572 and by the State of Hawai’i.

This work was made possible by utilizing the CANDIDE cluster at the Institut d’Astrophysique de Paris, which was funded through grants from the PNCG, CNES, DIM-ACAV, and the Cosmic Dawn Center and maintained by S. Rouberol.

This work was supported in part by the Canadian Advanced Network for Astronomical Research (CANFAR) and Compute Canada facilities.

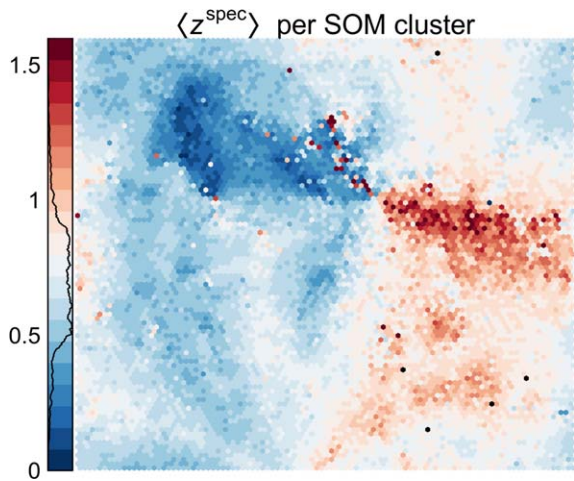
Funding for the SDSS has been provided by the Alfred P. Sloan Foundation, the Heising-Simons Foundation, the National Science Foundation, and the Participating Institutions. SDSS acknowledges support and resources from the Center for High-Performance Computing at the University of Utah. The SDSS website is www.sdss.org.

Appendix A

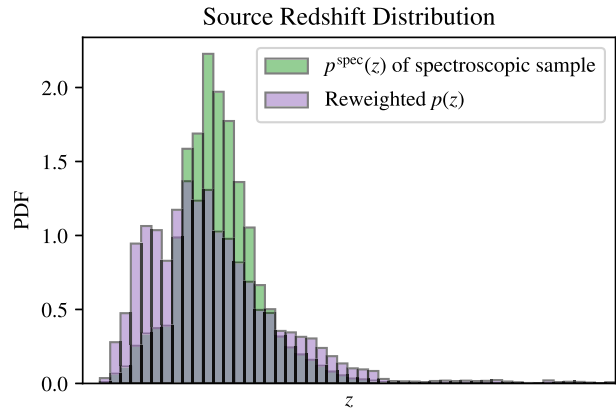
Estimation of the Source Redshift Distribution

From UNIONS r -band observations, we follow three steps to estimate the redshift distribution of our weak-lensing source sample. The first step is assigning multiband photometry to UNIONS galaxies. Using the overlap of UNIONS r -band

¹⁹ <https://pfs.ipmu.jp/>



(a) The SOM colour-coded in the mean redshift of the spectroscopic sample



(b) The blinded source redshift distributions

Figure 4. In panel (a), the trained SOM colored by the counts of the spectroscopic sample is shown. In panel (b), the redshift distributions $p^{\text{spec}}(z)$ and $p(z)$ are plotted with green and purple bars, respectively. The x -axis values are not shown according to the blinding policy of the UNIONS weak-lensing group.

observations with the Canada–France–Hawaii Telescope Lensing Survey (CFHTLenS; Heymans et al. 2012; Erben et al. 2013) W3 field ($\sim 44.2 \text{ deg}^2$), we assign $ugriz$ magnitudes by cross-matching. This can be done since CFHTLenS has deeper photometry (Hildebrandt et al. 2012) than UNIONS; basically, all CFIS (UNIONS r -band) objects are also visible in CFHTLenS, and the underlying redshift distribution is assumed to be the same after matching.

We calibrate the redshift distribution with spectroscopic calibration samples, which are constructed from DEEP2 (DEEP2 Galaxy Redshift Survey; Newman et al. 2013), VIMOS Very Large Telescope Deep Survey (VVDS; Le Fèvre et al. 2005), and VIMOS Public Extragalactic Redshift Survey (VIPERS; Scodreggio et al. 2018). These surveys are also observed with CFHTLenS $ugriz$ photometry. With the multi-band photometry of the spectroscopic sample, we then train SOMs (Kohonen 1982; Masters et al. 2015) to organize the sample in high-dimensional magnitude space. The SOM splits the matched sample into subsamples in its so-called SOM cells. The initial SOM cell grid has a resolution of 101×101 cells and is then hierarchically clustered into 5000 resolution elements for reliable statistics later on, shown in Figure 4. We then populate the SOM with the UNIONS weak-lensing sources with $ugriz$ photometry.

For every SOM cell i , a weight w_i^{SOM} is defined, which is the ratio of the number of UNIONS objects (weighted by their shape weights) over the number of spectroscopic objects (Wright et al. 2020). Finally, we get the UNIONS $p(z)$ by reweighting the spectroscopic redshift distribution $p^{\text{spec}}(z)$ according to the weights w_i^{SOM} in the i th SOM cells (Wright et al. 2020),

$$p(z) = \int w_i^{\text{SOM}}(z) p^{\text{spec}}(z) dz = \sum w_i^{\text{SOM}} p_i^{\text{spec}}(z), \quad (\text{A1})$$

where $p_i^{\text{spec}}(z)$ is the histogram of spectroscopic objects per SOM cell i . $p^{\text{spec}}(z)$ and $p(z)$ are shown in Figure 4.

Appendix B Black Hole Mass Systematic Tests

B.1. Type I AGN

As Liu et al. (2019) and Wu & Shen (2022) adopt different black hole mass prescriptions and only the former applies a host-galaxy contribution correction to the continuum luminosity, we perform several tests to examine the consistency of black hole masses from the catalogs. The two catalogs have duplicates at $z < 0.35$. In this redshift range and in the UNIONS-SDSS overlap region, there are 3383 AGNs only in Liu et al. (2019), 1482 only in Wu & Shen (2022), and 707 duplicates. We compare the black hole mass measurements from two catalogs for the duplicates and find that they are consistent within 1σ .

We try three methods to merge the samples. As our fiducial choice, we merge the two catalogs without extra correction (for the duplicates, we adopt Liu et al. 2019’s black hole masses). In this case, the fraction of black hole masses from Liu et al. (2019) in three bins (after merging) are 37.8%, 20.5%, and 12.5% for three mass bins, respectively. Based on the fiducial choice, we further use the Ho & Kim (2015) and Vestergaard & Peterson (2006) prescriptions, respectively, to infer black hole masses from the continuum luminosity and broad $H\beta$ line width provided by the catalogs. Following the same binning scheme and measurement pipeline, we find the difference in average black hole mass among the three merging methods to be less than 0.01 dex, and the lensing signals are indistinguishable. We conclude that the differences between the two catalogs have no significant effect on our claim.

B.2. Type II AGN

Black hole mass from single-spectrum velocity dispersion is affected by the fiber aperture. Thus, a proper aperture correction is needed for an accurate black hole mass estimate. The empirical relation we use to correct for the aperture effect of the velocity dispersion stems from a sample of early-type galaxies (Cappellari et al. 2006). However, our type II sample contains galaxies of

various types, raising the question of the validity of the derived black hole masses for this sample. As a consistency check, we restrict the type II sample to early-type galaxies, as follows. We use two different selection criteria to create early-type galaxy samples: (1) Sérsic index $n > 2.5$; (2) morphology parameter $T_{\text{Type}} < 0$ in the deep-learning-based catalog from Domínguez Sánchez et al. (2018). In both cases we obtain similar black hole-to-halo mass relations albeit with larger errors. Thus, the morphology of galaxies does not affect our conclusions.

Appendix C Systematic Tests for Galaxy–Galaxy Lensing Measurements

To validate our galaxy–galaxy lensing measurement, we conducted two null tests and measured the boost factor.

C.1. Cross-shear ($\Delta\Sigma_{\times}$) Test

Weak gravitational lensing does not produce shape distortions in the cross direction; therefore, the cross component of the shear γ_{\times} or “cross ESD” $\Delta\Sigma_{\times}$ is expected to be zero in the absence of systematics. Thus, $\Delta\Sigma_{\times}$ can be interpreted as a null test of systematics in the lensing-measurement process. We measure $\Delta\Sigma_{\times}$ with the same method and sample as for $\Delta\Sigma$,

$$\langle \Delta\Sigma(R)_{\times}^w \rangle = \frac{\sum_{l_s} w_l \overline{\Sigma_{cr}^{-1}}(z_l) w_s \epsilon_{\times,s} 1_b(R)(|\mathbf{r}_l - \mathbf{r}_s|)}{\sum_{l_s} w_l w_s (\overline{\Sigma_{cr}^{-1}}(z_l))^2}. \quad (\text{C1})$$

The results of the $\Delta\Sigma_{\times}$ test are shown in Figure 5. All data points are consistent with zero at 3σ , and $\sim 70\%$ are zero within 1σ . The reduced χ^2 values $\chi_{\text{dof}}^2(\Delta\Sigma_{\times})$ of the three bins are 1.06 (0.82), 0.45 (0.66), and 1.24 (0.71) for ShapePipe (*lensfit*). No evidence is found of any significant systematic errors.

C.2. Random Lens Test

We also measure lensing signals around a random sample as a null test. This sample is constructed by randomly sampling the SDSS footprint and then selecting the subsample in the sky region overlapping with UNIONS. To match the redshift distribution, we randomly assign the redshifts of the high-mass bin lens sample (the other two bins have the same $p(z)$ after weighting) to the random sample. Our random sample contains 543,402 random points.

Following the same procedure as before, we measure both tangential and cross components with respect to the random sample with the ShapePipe and *lensfit* shape catalogs. The results are presented in Figure 5. The lensing signals are in good consistency with zero. ShapePipe (*lensfit*) has a reduced χ^2 $\chi_{\text{dof}}^2(\Delta\Sigma_r)$ of 1.64 (0.92) in the tangential component and $\chi_{\text{dof}}^2(\Delta\Sigma_r) = 1.12$ (0.93) in the cross component. These values are consistent with the null hypothesis, indicating that systematic errors in the measurement are not significant.

C.3. Boost Factor

Galaxy–galaxy lensing signals are diluted by galaxies physically associated with lens galaxies, whose shapes are not affected by lensing. Since we cannot exclude these galaxies without photo- z in this work, it is important to quantify this effect. With the same random sample as in the random lens test, we calculate the boost factor (Hirata et al. 2004), which is defined as $B(r) = (N_{rs} \sum_{l_s} w_{l_s}) / (N_{ls} \sum_{rs} w_{rs})$, where N_{ls} and N_{rs} are the number of lens–source pairs and random–source pairs, respectively, and w_{ls} and w_{rs} are corresponding lensing weights. The results are shown in Figure 5. We apply the boost factor correction to the lensing signals we use in this work.

C.4. Influence of Redshift Calibration Uncertainty

Because we do not have an accurate estimate of the redshift calibration uncertainty to date, we use a simple method to test the dependence of our results on photo- z errors. We artificially shift the redshift-distribution function of the source sample by

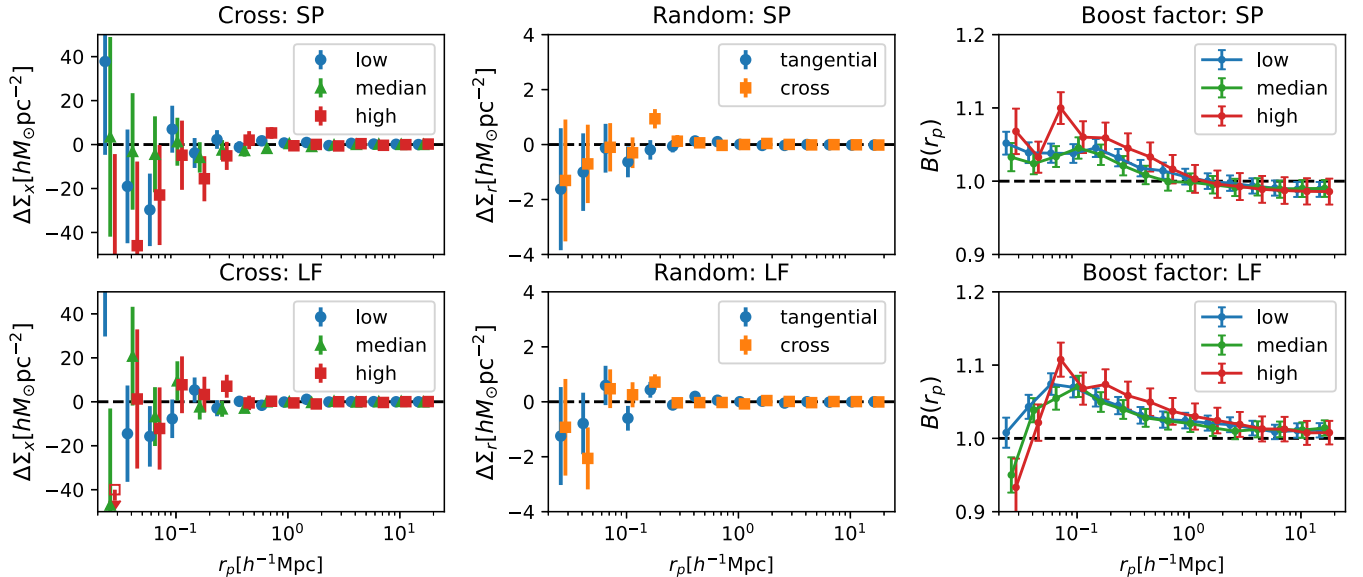


Figure 5. Systematic tests of lensing measurements. The top (bottom) column shows tests for ShapePipe (*lensfit*). The left two panels correspond to $\Delta\Sigma_{\times}$. Low-, medium-, and high-mass bins of type I sample are shown in blue circles, green triangles, and red rectangles in each panel. The middle two panels show the ESD and cross ESD around a random sample. The right two panels present the boost factor of the type I sample. Low-, medium-, and high-mass bins are shown in blue, green, and red points. In all panels, some results are slightly displaced in the x -direction to make the figure clear.

0.05, which is a very conservative estimate of the error, and remeasure the ESD. The change due to the shifted redshift distribution is less than 10%. The change in the inferred black hole–halo mass relation is less than 0.1dex, which is much smaller than the error of the halo mass measurement. The shape of the relation does not change.

Appendix D Details of the HOD Model

D.1. Baryonic Contribution

For source–lens separations (at the lens redshifts) that are much larger than the size of a typical galaxy, that galaxy can be considered as a point mass. The baryonic contribution to the ESD, which contains stars, dust, and gas, can then be written as

$$\Delta\Sigma_b(R) = \frac{M_*}{\pi R^2}. \quad (\text{D1})$$

For the type I sample, M_* is left as a free parameter. For the type II sample, M_* is fixed to the mean stellar mass of each bin from the MPA–JHU catalog.

D.2. One-halo Central-galaxy Contribution

We adopt a Navarro–Frenk–White (NFW) model to describe the density profile of the host halo for central galaxies,

$$\rho(r) = \frac{\rho_0}{(r/r_s)(1+r/r_s)^2}, \quad (\text{D2})$$

with $\rho_0 = 200 \rho_m / (3I_c)$ and $I_c = c^{-3} \int_0^c dx x(1+x)^{-2}$. Here, ρ_m is the mean density of the Universe, and c is the halo concentration parameter, defined as the ratio between the virial radius r_{200} and scale radius r_s of the halo, $c = r_{200}/r_s$. In this work, the concentration c is fixed by adopting the Duffy et al. (2008) concentration–mass relation. Assuming that the halo center is located at the central galaxy, the ESD $\Delta\Sigma_{\text{NFW}}$ of the halo within a disk of radius R is

$$\begin{aligned} \Delta\Sigma_{\text{h, cen}}(R) &= \Delta\Sigma_{\text{NFW}}(R) = \bar{\Sigma}_{\text{NFW}}(<R) - \Sigma_{\text{NFW}}(R) \\ &= \frac{M_h}{2\pi r_s^2 I} [g(R/r_s) - f(R/r_s)], \end{aligned} \quad (\text{D3})$$

where M_h is the halo mass. The functions $f(x)$ and $g(x)$ are defined as

$$\begin{aligned} f(x) &= \begin{cases} \frac{1}{x^2-2} \left[1 - \frac{\ln[(1+\sqrt{1-x^2})/x]}{\sqrt{1-x^2}} \right], & x < 1 \\ \frac{1}{3}, & x = 1, \\ \frac{1}{x^2-1} \left[1 - \frac{\arctan(\sqrt{x^2-1})}{\sqrt{x^2-1}} \right]; & x > 1 \end{cases} \\ g(x) &= \begin{cases} \frac{2}{x^2} \left[\ln x/2 + \frac{\ln[(1+\sqrt{1-x^2})/x]}{\sqrt{1-x^2}} \right], & x < 1 \\ 2 - 2 \ln 2, & x = 1. \\ \frac{2}{x^2} \left[\ln x/2 + \frac{\arctan(\sqrt{x^2-1})}{\sqrt{x^2-1}} \right], & x > 1 \end{cases} \end{aligned} \quad (\text{D4})$$

D.3. One-halo Satellite Galaxy Contribution

We use the NFW model also for the host halo of satellites. Compared to the central-galaxy term, the satellite halo has a

spatial offset. First, the excesses surface density, given the projected distance between the satellite galaxy and the halo center, R_{sat} , is

$$\begin{aligned} \Delta\Sigma_{\text{off}}(R|M_{\text{h, sat}}, R_{\text{sat}}) &= \frac{1}{2\pi} \int_0^{2\pi} \Delta\Sigma_{\text{NFW}} \\ &\times ((R^2 + R_{\text{sat}}^2 + 2RR_{\text{sat}} \cos \theta)^{\frac{1}{2}} |M_{\text{h, sat}}) d\theta. \end{aligned} \quad (\text{D5})$$

We integrate this equation over the distribution functions of $M_{\text{h, sat}}$ and R_{sat} to obtain the effective one-halo satellite term as

$$\begin{aligned} \Delta\Sigma_{\text{h, sat}}(R) &= \iint \Delta\Sigma_{\text{off}}(R|M_{\text{h, sat}}, R_{\text{sat}}) \\ &\times P(R_{\text{sat}}|M_{\text{h, sat}})P(M_{\text{h, sat}})dR_{\text{sat}}dM_{\text{h, sat}}. \end{aligned} \quad (\text{D6})$$

We assume that satellite galaxies follow the spatial distribution of dark matter, which is the NFW density profile. We set

$$\begin{aligned} P(R_{\text{sat}}|M_{\text{h, sat}}) &\propto \Sigma_{\text{NFW}}(R_{\text{sat}}, M_{\text{h, sat}}) \cdot 2\pi R_{\text{sat}} dR_{\text{sat}} \\ &= \frac{M_{\text{h, sat}}}{2\pi r_s^2(M_{\text{h, sat}})I} f[R_{\text{sat}}/r_s(M_{\text{h, sat}})] \cdot 2\pi R_{\text{sat}} dR_{\text{sat}}. \end{aligned} \quad (\text{D7})$$

Following Guzik & Seljak (2002), we use an HOD model to infer

$$\begin{aligned} P(M_{\text{h, sat}}|M_{\text{sub}}) &\propto P(M_{\text{sub}}|M_{\text{h, sat}})P(M_{\text{h, sat}}) \\ &\propto \langle N_{\text{sat}}(M_{\text{h, sat}}) \rangle F_h(M_{\text{h, sat}}), \end{aligned} \quad (\text{D8})$$

where $F_h(M_h)$ is the halo mass function and $\langle N_{\text{sat}}(M_h) \rangle$ is the halo occupation function of satellite galaxies. In this work, we use the halo mass function from Tinker et al. (2008) and the HOD model from Guzik & Seljak (2002).

D.3.1. Two-halo Term

For the two-halo term, we use the Tinker et al. (2010) halo bias model to infer the halo–matter correlation function $\xi_{\text{hm}} = b_h \xi_{\text{mm}}$ based on the dark-matter correlation function ξ_{mm} . From that, we can calculate the surface density as












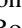

$$\Sigma_{2\text{h}}(R) = b_h(M_{\text{h, cen}}) \times 2\bar{p} \int_R^\infty \xi_{\text{mm}}(r) \frac{rdr}{\sqrt{r^2 - R^2}}. \quad (\text{D9})$$

D.4. Lens Model Validation

To validate the model, we cross-match the type II sample with the Yang et al. (2007) SDSS group catalog to select a purely central-galaxy subsample. Subsequently, we measure the ESD for both the type II sample and the central-galaxy subsample using the ShapePipe catalog. Next, we fit the central-galaxy subsample lensing signals with the lens model (Section 3.3) but set the satellite fraction to zero. This allows us to make two consistency tests. First, we compare the contributions of central galaxies from the entire type II sample by using the best-fit central ESD term to the ESD measured from the central-galaxy subsample. We find that they are broadly consistent. Second, we compare the inferred halo masses. They are consistent within 1σ across all mass ranges considered in this work, indicating that our lens model is reliable.

ORCID iDs

Qinxun Li  <https://orcid.org/0000-0003-3616-6486>
Martin Kilbinger  <https://orcid.org/0000-0001-9513-7138>
Wentao Luo  <https://orcid.org/0000-0003-1297-6142>

Kai Wang  <https://orcid.org/0000-0002-3775-0484>
 Huiyuan Wang  <https://orcid.org/0000-0002-4911-6990>
 Anna Wittje  <https://orcid.org/0000-0002-8173-3438>
 Hendrik Hildebrandt  <https://orcid.org/0000-0002-9814-3338>
 Ludovic Van Waerbeke  <https://orcid.org/0000-0002-2637-8728>
 Michael J. Hudson  <https://orcid.org/0000-0002-1437-3786>
 Samuel Farrens  <https://orcid.org/0000-0002-9594-9387>
 Tóibias I. Liaudat  <https://orcid.org/0000-0002-9104-314X>
 Huiling Liu  <https://orcid.org/0009-0008-6273-8269>
 Ziwen Zhang  <https://orcid.org/0000-0002-9272-5978>
 Lucie Baumont  <https://orcid.org/0000-0002-1518-0150>
 Thomas de Boer  <https://orcid.org/0000-0001-5486-2747>
 Jiaqi Wang  <https://orcid.org/0000-0003-0086-790X>

References

- Baes, M., Buyle, P., Hau, G. K. T., & Dejonghe, H. 2003, *MNRAS*, **341**, L44
 Baldwin, J. A., Phillips, M. M., & Terlevich, R. 1981, *PASP*, **93**, 5
 Bandara, K., Crampton, D., & Simard, L. 2009, *ApJ*, **704**, 1135
 Bentz, M. C., Peterson, B. M., Pogge, R. W., Vestergaard, M., & Onken, C. A. 2006, *ApJ*, **644**, 133
 Bertin, E. 2011, in ASP Conf. Ser. 442, *Astronomical Data Analysis Software and Systems XX*, ed. I. N. Evans et al. (San Francisco, CA: ASP), 435
 Blanton, M. R., Schlegel, D. J., Strauss, M. A., et al. 2005, *AJ*, **129**, 2562
 Brinchmann, J., Charlot, S., White, S. D. M., et al. 2004, *MNRAS*, **351**, 1151
 Cappellari, M., Bacon, R., Bureau, M., et al. 2006, *MNRAS*, **366**, 1126
 Davé, R., Anglés-Alcázar, D., Narayanan, D., et al. 2019, *MNRAS*, **486**, 2827
 Davis, B. L., Graham, A. W., & Combes, F. 2019, *ApJ*, **877**, 64
 Dey, A., Schlegel, D. J., Lang, D., et al. 2019, *AJ*, **157**, 168
 Domínguez Sánchez, H., Huertas-Company, M., Bernardi, M., Tuccillo, D., & Fischer, J. L. 2018, *MNRAS*, **476**, 3661
 Dressler, A., & Richstone, D. O. 1988, *ApJ*, **324**, 701
 Du, P., & Wang, J.-M. 2019, *ApJ*, **886**, 42
 Duffy, A. R., Schaye, J., Kay, S. T., & Dalla Vecchia, C. 2008, *MNRAS*, **390**, L64
 Erben, T., Hildebrandt, H., Miller, L., et al. 2013, *MNRAS*, **433**, 2545
 Euclid Collaboration, Blanchard, A., Camera, S., et al. 2020, *A&A*, **642**, A191
 Farrens, S., Guinot, A., Kilbinger, M., et al. 2022, *A&A*, **664**, A141
 Ferrarese, L. 2002, *ApJ*, **578**, 90
 Ferrarese, L., & Merritt, D. 2000, *ApJL*, **539**, L9
 Foreman-Mackey, D., Hogg, D. W., Lang, D., & Goodman, J. 2013, *PASP*, **125**, 306
 Gao, L., & White, S. D. M. 2007, *MNRAS*, **377**, L5
 Gebhardt, K., Bender, R., Bower, G., et al. 2000, *ApJL*, **539**, L13
 Gong, Y., Liu, X., Cao, Y., et al. 2019, *ApJ*, **883**, 203
 GRAVITY Collaboration, Amorim, A., Bourdarot, G., et al. 2024, *A&A*, **684**, A167
 Guinot, A., Kilbinger, M., Farrens, S., et al. 2022, *A&A*, **666**, A162
 Guzik, J., & Seljak, U. 2002, *MNRAS*, **335**, 311
 Houbouzit, M., Li, Y., Somerville, R. S., et al. 2021, *MNRAS*, **503**, 1940
 Heymans, C., Van Waerbeke, L., Miller, L., et al. 2012, *MNRAS*, **427**, 146
 Hildebrandt, H., Erben, T., Kuijken, K., et al. 2012, *MNRAS*, **421**, 2355
 Hirata, C. M., Mandelbaum, R., Seljak, U., et al. 2004, *MNRAS*, **353**, 529
 Ho, L. C., & Kim, M. 2015, *ApJ*, **809**, 123
 Ivezić, Ž., Kahn, S. M., Tyson, J. A., et al. 2019, *ApJ*, **873**, 111
 Kauffmann, G., Heckman, T. M., White, S. D. M., et al. 2003, *MNRAS*, **341**, 33
 Kilbinger, M. 2015, *RPPh*, **78**, 086901
 Kohonen, T. 1982, *Biol. Cybern.*, **43**, 59
 Kormendy, J., & Bender, R. 2011, *Natur*, **469**, 377
 Kormendy, J., & Ho, L. C. 2013, *ARA&A*, **51**, 511
 Kormendy, J., & Richstone, D. 1995, *ARA&A*, **33**, 581
 Krumpe, M., Miyaji, T., Georgakakis, A., et al. 2023, *ApJ*, **952**, 109
 Krumpe, M., Miyaji, T., Husemann, B., et al. 2015, *ApJ*, **815**, 21
 Le Fèvre, O., Vettolani, G., Garilli, B., et al. 2005, *A&A*, **439**, 845
 Leauthaud, A. J., Benson, A., Civano, F., et al. 2015, *MNRAS*, **446**, 1874
 Levi, M., Bebek, C., Beers, T., et al. 2013, arXiv:1308.0847
 Liaudat, T., Bonnin, J., Starck, J.-L., et al. 2021, *A&A*, **646**, A27
 Liu, H.-Y., Liu, W.-J., Dong, X.-B., et al. 2019, *ApJS*, **243**, 21
 Luo, W., Silverman, J. D., More, S., et al. 2022, arXiv:2204.03817
 Luo, W., Yang, X., Lu, T., et al. 2018, *ApJ*, **862**, 4
 Lyke, B. W., Higley, A. N., McLane, J. N., et al. 2020, *ApJS*, **250**, 8
 Magorrian, J., Tremaine, S., Richstone, D., et al. 1998, *AJ*, **115**, 2285
 Mandelbaum, R., Li, C., Kauffmann, G., & White, S. D. M. 2009, *MNRAS*, **393**, 377
 Mandelbaum, R., Seljak, U., Kauffmann, G., Hirata, C. M., & Brinkmann, J. 2006, *MNRAS*, **368**, 715
 Marasco, A., Cresci, G., Posti, L., et al. 2021, *MNRAS*, **507**, 4274
 Masters, D., Capak, P., Stern, D., et al. 2015, *ApJ*, **813**, 53
 McConnell, N. J., & Ma, C.-P. 2013, *ApJ*, **764**, 184
 Miller, L., Kitching, T. D., Heymans, C., Heavens, A. F., & van Waerbeke, L. 2007, *MNRAS*, **382**, 315
 Mo, H., Chen, Y., & Wang, H. 2023, arXiv:2311.05030
 Newman, J. A., Cooper, M. C., Davis, M., et al. 2013, *ApJS*, **208**, 5
 Pizzella, A., Corsini, E. M., Dalla Bontà, E., et al. 2005, *ApJ*, **631**, 785
 Planck Collaboration, Aghanim, N., Akrami, Y., et al. 2020, *A&A*, **641**, A6
 Powell, M. C., Allen, S. W., Caglar, T., et al. 2022, *ApJ*, **938**, 77
 Powell, M. C., Cappelluti, N., Urry, C. M., et al. 2018, *ApJ*, **858**, 110
 Robinson, J. H., Bentz, M. C., Courtois, H. M., et al. 2021, *ApJ*, **912**, 160
 Sabra, B. M., Saliba, C., Akl, M. A., & Chahine, G. 2015, *ApJ*, **803**, 5
 Saglia, R. P., Opitsch, M., Erwin, P., et al. 2016, *ApJ*, **818**, 47
 Schaye, J., Crain, R. A., Bower, R. G., et al. 2015, *MNRAS*, **446**, 521
 Scodieggio, M., Guzzo, L., Garilli, B., et al. 2018, *A&A*, **609**, A84
 Shankar, F., Allevato, V., Bernardi, M., et al. 2020, *NatAs*, **4**, 282
 Shen, Y. 2013, *BASI*, **41**, 61
 Shen, Y., Richards, G. T., Strauss, M. A., et al. 2011, *ApJS*, **194**, 45
 Shimasaku, K., & Izumi, T. 2019, *ApJL*, **872**, L29
 Spergel, D., Gehrels, N., Baltay, C., et al. 2015, arXiv:1503.03757
 Springel, V., Pakmor, R., Pillepich, A., et al. 2017, *MNRAS*, **475**, 676
 Tinker, J., Kravtsov, A. V., Klypin, A., et al. 2008, *ApJ*, **688**, 709
 Tinker, J. L., Robertson, B. E., Kravtsov, A. V., et al. 2010, *ApJ*, **724**, 878
 Vestergaard, M., & Peterson, B. M. 2006, *ApJ*, **641**, 689
 Voit, G. M., Oppenheimer, B. D., Bell, E. F., Terrazas, B., & Donahue, M. 2024, *ApJ*, **960**, 28
 Volonteri, M., Natarajan, P., & Gültekin, K. 2011, *ApJ*, **737**, 50
 Wang, K., Mo, H. J., Chen, Y., et al. 2024, *MNRAS*, **528**, 2046
 Wechsler, R. H., & Tinker, J. L. 2018, *ARA&A*, **56**, 435
 WFST Collaboration, Wang, T., Liu, G., et al. 2023, *SCPMA*, **66**, 109512
 Wright, A. H., Hildebrandt, H., van den Busch, J. L., & Heymans, C. 2020, *A&A*, **637**, A100
 Wu, Q., & Shen, Y. 2022, *ApJS*, **263**, 42
 Yang, X., Mo, H. J., & van den Bosch, F. C. 2008, *ApJ*, **676**, 248
 Yang, X., Mo, H. J., van den Bosch, F. C., et al. 2007, *ApJ*, **671**, 153
 Zhang, H., Behroozi, P., Volonteri, M., et al. 2024, *MNRAS*, **529**, 2777
 Zhang, H., Behroozi, P., Volonteri, M., et al. 2023, *MNRAS*, **518**, 2123
 Zhang, J., Liu, C., Vaquero, P. A., et al. 2022, *AJ*, **164**, 128
 Zhang, Z., Wang, H., Luo, W., et al. 2024, *ApJ*, **960**, 71
 Zhu, K., Li, R., Cao, X., et al. 2023, *RAA*, **23**, 085001